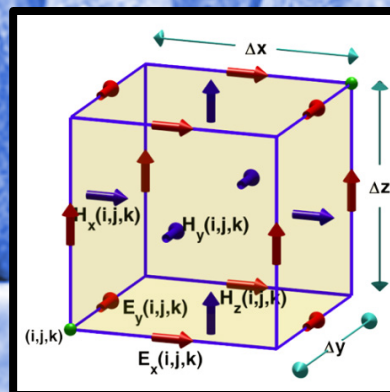
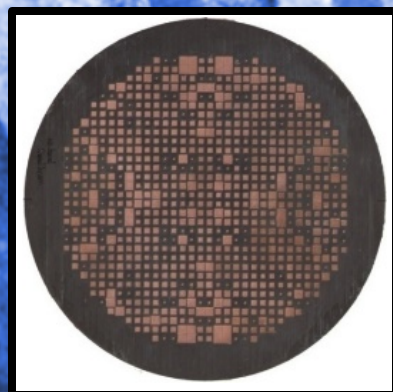


Selected Cover Image

The figure shows a schematic diagram of a tapered slot antenna (top) and a photograph of the physical antenna (middle). The schematic includes labels for 'Corrugation', 'Top', 'Bottom', 'Dielectric Loading', 'Microstrip to SIW transition', and various dimensions like $L1, L2, L3, L4$ and $W1, W2, W3, W4, W5$. The photograph shows a tapered slot antenna on a substrate, with a ruler below it for scale.

A color plot showing the E-field distribution along the length of the antenna. The color scale ranges from 1.1125e+003 (blue) to 1.1125e+005 (red). The plot shows a localized high-field region at the narrow end of the tapered slot.

Nishesh Tiwari and Thipparaju R. Rao
A Substrate Integrated Waveguide Based Antipodal Linear Tapered Slot Antenna for 60 GHz Wireless Communications



APPLIED COMPUTATIONAL ELECTROMAGNETICS SOCIETY EXPRESS JOURNAL

<http://aces-society.org>

GENERAL INFORMATION

PURPOSE AND SCOPE: The Applied Computational Electromagnetics Society (*ACES*) *Express* Journal hereinafter known as the *ACES Express Journal* is devoted to the timely and rapid exchange of information in computational electromagnetics, to the advancement of the state-of-the art, and the promotion of related technical activities. The primary objective of the information exchange is to inform the scientific community in a short amount of time on the developments of recent computational electromagnetics tools and their use in electrical engineering, physics, or related areas. The technical activities promoted by this publication include code validation, performance analysis, and input/output standardization; code or technique optimization and error minimization; innovations in solution technique or in data input/output; identification of new applications for electromagnetics modeling codes and techniques; integration of computational electromagnetics techniques with new computer architectures; and correlation of computational parameters with physical mechanisms.

SUBMISSIONS: The *ACES Express Journal* welcomes original, previously unpublished papers, relating to applied computational electromagnetics. Typical papers will represent the computational electromagnetics aspects of research in electrical engineering, physics, or related disciplines as well as research in the field of applied computational electromagnetics.

Manuscripts are to be submitted through the upload system of *ACES* web site <http://aces-society.org>. Please see "Information for Authors" on inside of back cover and at *ACES* web site. For additional information contact the Editor-in-Chief:

Dr. Ozlem Kilic

Department of Electrical Engineering and Computer Science
The Catholic University of America
Washington, DC 20064
Email: kilic@cua.edu

SUBSCRIPTIONS: All members of the Applied Computational Electromagnetics Society are entitled to access and download the *ACES Express Journal* of any published journal article available at <http://aces-society.org>. *ACES Express Journal* is an online journal and printed copies are not available. Subscription to *ACES* is through the web site.

LIABILITY. Neither *ACES*, nor the *ACES Express Journal* editors, are responsible for any consequence of misinformation or claims, express or implied, in any published material in an *ACES Express Journal* issue. This also applies to advertising, for which only camera-ready copies are accepted. Authors are responsible for all information contained in their papers. If any material submitted for publication includes material which has already been published elsewhere, it is the author's responsibility to obtain written permission to reproduce such material.

THE APPLIED COMPUTATIONAL ELECTROMAGNETICS SOCIETY

<http://aces-society.org>

EDITOR-IN-CHIEF

Ozlem Kilic

Department of Electrical Engineering and Computer Science
The Catholic University of America
Washington, DC 20064

ASSOCIATE EDITORS-IN-CHIEF

Lijun Jiang

University of Hong Kong, Dept. of EEE
Hong, Kong

Steven J. Weiss

US Army Research Laboratory
Adelphi Laboratory Center (RDRL-SER-M)
Adelphi, MD 20783, USA

Amedeo Capozzoli

Universita di Napoli Federico II, DIETI
I-80125 Napoli, Italy

Shinichiro Ohnuki

Nihon University
Tokyo, Japan

William O'Keefe Coburn

US Army Research Laboratory
Adelphi Laboratory Center (RDRL-SER-M)
Adelphi, MD 20783, USA

Yu Mao Wu

Fudan University
Shanghai 200433, China

Kubilay Sertel

The Ohio State University
Columbus, OH 43210, USA

Jiming Song

Iowa State University, ECE Dept.
Ames, IA 50011, USA

Maokun Li

Tsinghua University, EE Dept.
Beijing 100084, China

EDITORIAL ASSISTANTS

Toan K. Vo Dai

The Catholic University of America, EECS Dept.
Washington, DC 20064, USA

Shanell Lopez

Colorado School of Mines, EECS Dept.
Golden, CO 80401, USA

AUGUST 2016 REVIEWERS

William Coburn

Vivek Dhoot

Mang He

Quang Nguyen

Nghia Tran

Nurhan Turker Tokan

Arash Valizade Shahmirzadi

**THE APPLIED COMPUTATIONAL ELECTROMAGNETICS SOCIETY
EXPRESS JOURNAL**

Vol. 1 No. 8

August 2016

TABLE OF CONTENTS

“Multi-level Fast Multipole Algorithm for 3-D Homogeneous Dielectric Objects
Using MPI-CUDA on GPU Cluster”
Tuan Phan, Nghia Tran, and Ozlem Kilic..... 216

“A Substrate Integrated Waveguide Based Antipodal Linear Tapered Slot
Antenna for 60 GHz Wireless Communications”
Nishesh Tiwari and Thipparaju R. Rao..... 220

“Installed Antenna Performance in Airborne Radomes of Different Profiles”
Ana Vukovic, Phillip Sewell, Xuesong Meng, and Trevor M. Benson.....224

“A Compact Fractal Monopole Antenna with Defected Ground Structure for Wideband
Communication”
Ankan Bhattacharya, Bappaditya Roy, Santosh K. Chowdhury,
and Anup K. Bhattacharjee..... 228

Multi-level Fast Multipole Algorithm for 3-D Homogeneous Dielectric Objects Using MPI-CUDA on GPU Cluster

Tuan Phan, Nghia Tran, and Ozlem Kilic

Department of Electrical Engineering and Computer Science
The Catholic University of America, Washington, DC, 20064, USA
30phan@cua.edu, 16tran@cua.edu, kilic@cua.edu

Abstract — The implementation of Multi-level Fast Multipole Algorithm (MLFMA) on a 13-node Graphical Processing Unit (GPU) cluster using Message Passing Interface (MPI) and CUDA programming is presented. The performance achievements are investigated in terms of accuracy, speed up, and scalability. The experimental results demonstrate that our MLFMA implementation on GPUs is much faster than (up to 66x) that of the CPU implementation without trading off the accuracy.

Index Terms — Graphics Processing Unit (GPU), Multilevel Fast Multipole Algorithm (MLFMA).

I. INTRODUCTION

In the last two decades, many authors have been investigating solving large scale electromagnetics problems using numerical techniques such as Method of Moments (MoM), Fast Multipole Method (FMM) and Multi-level Fast Multipole Algorithm (MLFMA). Modeling large-scale objects requires large memory resources and computational time. Among these methods, the MLFMA has the least computational complexity $O(N \log N)$, while MoM and FMM have the complexity of $O(N^3)$ and $O(N^{3/2})$, respectively.

MLFMA has successfully been implemented in parallel on CPU clusters to solve up to few hundreds millions of unknowns [1]. The CPU cluster-based parallel implementation has advantages of large memory resources, but their speed is relatively slow in comparison with GPU cluster-based implementations. In the past, our group has implemented a parallel version of MLFMA on GPUs clusters to solve for perfect electric conductor (PEC) objects [2]. This paper continues our efforts to investigate the implementation of MLFMA on GPU cluster platform for solving large scale dielectric objects. The platform we employ is a 13-node GPU cluster, which utilizes NVidia Tesla M2090 GPU. An MVAPICH2 implementation of Message Passing Interface (MPI) is used for parallel programming.

In this work, a workload partitioning technique, namely group-based distribution is investigated among

the 13 computing nodes. This technique is applied for the tree structure in MLFMA as will be discussed in details in the implementation section. The rest of the paper is organized as follows. An overview of MLFMA for homogeneous dielectric objects is provided in Section 2. Section 3 presents the parallel implementation of MLFMA on GPU clusters. Simulation results are discussed in Section 4, followed by the conclusions in Section 5.

II. OVERVIEW OF THE MULTILEVEL FAST MULTIPOLE ALGORITHM ON DIELECTRIC OBJECTS

In this section, we provide a brief overview to help our discussion on the parallel implementation of dielectric MLFMA, which is presented in Section III. Numerical techniques such as MoM, FMM, and MLFMA are invented to solve for the linear equation system $ZI = V$, where I represents the unknown currents, V depends on the incident field, and Z is the impedance matrix. For an arbitrary structure meshed with M -edges the conventional MoM requires the computation of all direct interactions among the edges ($M \times M$), while FMM accelerates the matrix-vector product by using an approximate multiple expansion of the fields to divide structure into near and far group interaction concept [3]. MLFMA is based on FMM, but it relies on forming hierarchical groupings to render reactions with far groups more efficiently. The main idea of the grouping concept of MLFMA is shown in Fig. 1, where M edges are categorized into an N -level tree structure. For the sake of simplicity and convenience, the oct-tree structure is used for grouping in MLFMA [4].

The near interactions among edges in spatially nearby groups are computed and stored using the conventional MoM [5], while the far interactions are calculated in a group-by-group manner consisting of three stages, namely, aggregation, translation, and disaggregation.

In our previous work on FMM for a homogeneous dielectric object (permittivity ϵ_2 , permeability μ_2)

immersed in an infinite homogeneous medium (permittivity ϵ_1 , permeability μ_1), the basic formulas are given as:

$$Z_{ij,JJ}^1 = \frac{\omega\mu k}{16\pi^2} \int d^2\hat{k} T_{r_m}^E(\hat{k}) T_L(k, \hat{k}, r_{ii}') \bullet R_{m_i'}^E(\hat{k}), \quad (1)$$

$$Z_{ij,MM}^1 = \frac{\omega\epsilon k \eta^2}{16\pi^2} \int d^2\hat{k} T_{r_m}^E(\hat{k}) T_L(k, \hat{k}, r_{ii}') \bullet R_{m_i'}^E(\hat{k}), \quad (2)$$

$$Z_{ij,MJ}^1 = \frac{k\eta}{16\pi^2} \int d^2\hat{k} T_{r_m}^{ED}(\hat{k}) T_L(k, \hat{k}, r_{ii}') \bullet R_{m_i'}^E(\hat{k}) \\ = -Z_{ij,JM}^1,$$

where

$$T_{r_m}^E = \int_S (\mathbf{I} - \hat{k}\hat{k}) \bullet \mathbf{f}_m(\mathbf{r}_{im}) e^{-jk \cdot \mathbf{r}_{im}} dS, \quad (4)$$

$$T_{r_m}^{ED} = \int_S \hat{k} \times \mathbf{f}_m(\mathbf{r}_{im}) e^{-jk \cdot \mathbf{r}_{im}} dS, \quad (5)$$

$$R_{m_i'}^E = \int_S \mathbf{f}_{m_i'}(\mathbf{r}_{m_i'}) e^{-jk \cdot \mathbf{r}_{m_i'}} dS, \quad (6)$$

$$T_L = \sum_{l=0}^L (-j)^l (2l+1) h_l^{(2)}(\mathbf{k} \bullet \mathbf{r}_{ii}') P_l(\hat{k} \bullet \mathbf{r}_{ii}'), \quad (7)$$

In the above equations, L denotes for multipole expansion number, $h_l^{(2)}$ identifies the second kind of Hankel function, P_l stands for Legendre polynomial of degree l terms. By the changing the sub and superscripts “1” to “2” in Equations (1) to (7), we can complete the 2N linear equations. The same idea applies for MLFMA to solve for dielectric object [6].

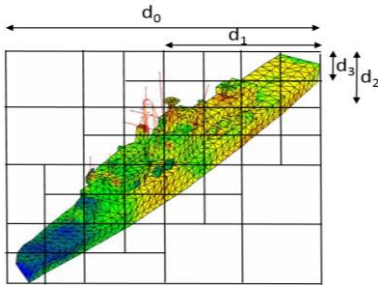


Fig. 1. MLFMA general grouping concepts.

III. GPU CLUSTER IMPLEMENTATION OF MLFMA

In this section, a detailed implementation of MLFMA is provided. The implementation is divided into three main blocks, which consist of pre-processing, processing and post-processing.

While the pre-processing and post processing processes utilize CPU, the processing are based on GPU cluster. The main purpose of the pre-processing step is to read the geometry mesh data, to set up the data structure, and to construct the oct-tree. Results from this process are transferred to the GPU memory, and the entire computation is performed on the GPU clusters. The user interested quantities such as scattered fields, radar cross section, are post-processing and handled on CPU. The processing step is the most time consuming in

the algorithm. Hence, we focus our parallel programming of MLFMA on the most computationally intensive step, i.e., the processing. The details of this process is shown in Fig. 2.

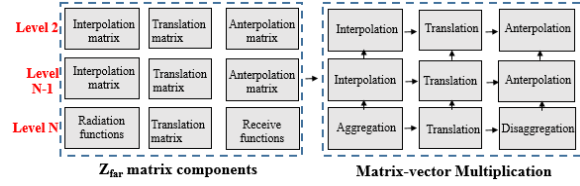


Fig. 2. A detail implementation of processing phase.

In the processing phase, the computational tasks are assigned to all computing nodes in a balanced manner such that each node holds the same amount of workload, and the inter-node communication is minimized. This is achieved by uniformly distributing the total number of groups of all levels except level 1 and 2, G , among the n computing nodes. We define this technique of data distribution among computing nodes as the group-based distribution. Two levels of parallelization are performed in this stage: among the n computing nodes using MPI library, and within the GPU per node using CUDA programming model. The CUDA thread-block model is utilized to calculate the assigned workload within a node. In this paper, only the far interactions is presented, and the near field and \mathbf{V} vector calculation implementations can be found in [7].

The GPU cluster used for this work has 13 computing nodes. Each node has a dual 6-core 2.66 GHz Intel Xeon processor, 48 GB RAM along with one NVidia Tesla M2090 GPU running at 1.3 GHz supported with 6GB of GPU memory. The nodes are interconnected through the InfiniBand interconnection. The cluster populates CUDA v6.0 and MVAPICH2 v1.8.1 (an implementation of MPI).

A. Far interactions calculations

There are five main steps in this stage: radiation functions, receive function, interpolation, anterpolation and translation matrices. The group-based technique is performed to calculate the radiation functions, receive functions, and translation matrices.

(i) Radiation and Receive Function Calculations

The calculation of the radiation, T^E , and receive, R^E , functions for Z^{far} matrix are similar since R^E is the complex conjugate of T^E . Following the G group distribution as mentioned above, each computing node handles the calculation of K directions for G_{node} groups.

(ii) Translation Matrix Calculation

The workload for the T_L calculations is also distributed across the n nodes using the group-based

technique. In order to save memory, each CUDA block is assigned to compute one sparse row of the T_L matrix for a given direction.

(iii) Interpolation and Anterpolation Matrices

Due to the differences of sampling frequencies among the levels of the oct-tree structure, the interpolation and anterpolation are required for the aggregation and disaggregation stages. In this task, each node will handle the calculations of $K_{children/node}$ rows of the interpolation matrix $K_{children} * K_{parent}$, where $K_{children}$ and K_{parent} are the number of directions of finer and coarser level, respectively. The blocks of a maximum of 1024 threads are utilized in the CUDA kernel once it is launched. The anterpolation is simply the transpose of the interpolation. Thus, their implementations are similar.

B. Matrix-vector multiplication

The matrix-vector multiplication (MVM) method is an important technique to accelerate the computational time, which can be found in detail in [8]. An iterative method; i.e., the biconjugate gradient stabilized method (BiCGSTAB), is used to solve for the linear system. The computation of $Z_{far}I$ is shown in Fig. 3, where the unknown current vector I is distributed among the 13 nodes using the group-based technique [9].

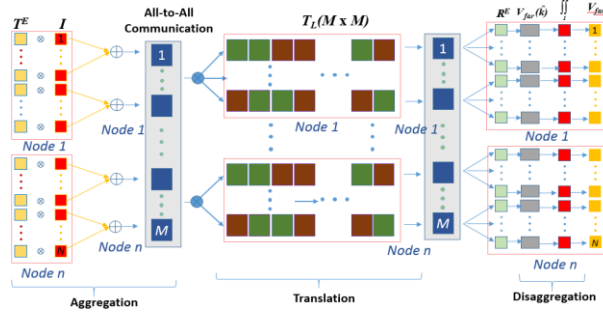


Fig. 3. The parallelization of matrix-vector multiplication for $Z_{far}I$.

First, in the aggregation stage, at level max, (N), each node computes the radiated fields for its assigned groups by multiplying the current I with the radiation functions, T^E , and accumulating within each group. Then, all-to-all communication is required to broadcast the data to all nodes. For the remaining levels (up to level 2), the radiated field is the result of multiplying interpolation matrices with radiated fields of its direct children groups.

In the translation stage, at each level (except levels 0 and 1) the radiated fields for each group are calculated by multiplying the translation matrix with the radiated fields.

In the disaggregation stage, going down from level 2 to level N, the radiated fields at each group are

added with the inherited fields from its parents using interpolation. At the maximum level (N), the received fields are multiplied with their corresponding receive functions, and integrated over K directions. Then, the near components and far components of MVM are incorporated to complete the full matrix. In the end of this process, the results from all nodes are summed and updated.

IV. EXPERIMENTAL RESULTS

A. Accuracy

The accuracy of the method is verified by comparing the Radar Cross Sections (RCSs) of 9λ -diameter dielectric sphere with analytical technique, Mie scattering, and a 10λ -height by 4λ -radius dielectric cone with commercial simulation software, FEKO. In two cases, the results verify our method's accuracy, as observed in Fig. 4 and Fig. 5, respectively.

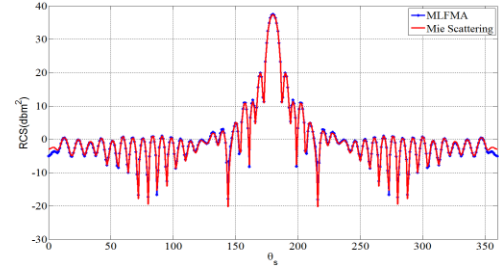


Fig. 4. RCS of a 9λ diameter dielectric sphere ($\epsilon = 4 - 0.1i$) with 105,000 unknowns.

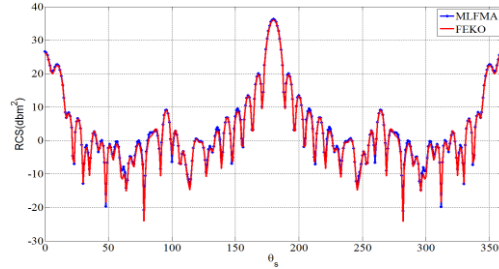


Fig. 5. RCS of 10λ height and 4λ radius dielectric cone ($\epsilon = 4 - 0.1i$) with 109,000 unknowns.

B. Performance on GPU cluster

We conducted two experiments to investigate the speed-up, scalability using a fixed-workload model (Amdahl's Law) and maximum problem size. The speed-up is defined as the ratio of time required by multi-node GPU implementation with respect to the 8-node CPU implementation. The scalability is the normalized speed-up of multiple nodes in reference to the speed-up of 8 nodes. Finally, we fully utilized the memory available of 13 nodes to investigate the maximum number of unknowns we can handle.

In the first experiment, a 16.74λ -diameter dielectric

sphere (320k unknowns) which requires the memory of at least 8 nodes is used. The results are evaluated in terms of speed-up and scalability. As shown in Fig. 6, the speed-up for process of matrix-vector products and matrix fill increases from 45.6 for 8 nodes to 66.4 for 13 nodes. The GPU execution time decreases as the number of nodes increases because of less workload per node.

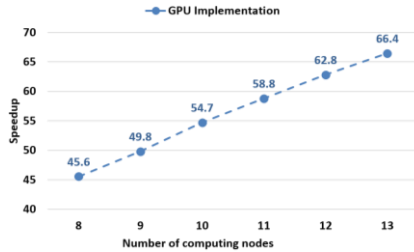


Fig. 6. Speedup analysis for the fixed-workload model (vs. 8 nodes CPU implementation, 100 iterations).

For the scalability, we keep the problem size constant and compare how the speed-up improves with increasing number of nodes, Fig. 7. It shows a good agreement between our implementation and the theoretical expectation.

In the second experiment, we try to solve for the largest problem size using the maximum memory available to us in each node. As the number of nodes increases, we increase the problem size to fully utilize the available memory. As shown in Fig. 8, we can process a maximum problem size of 439k unknowns with a speed-up of 46.

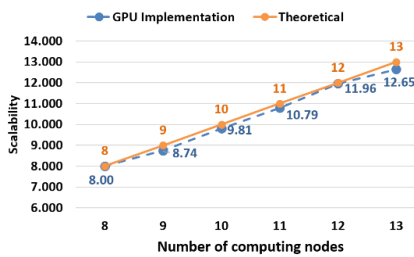
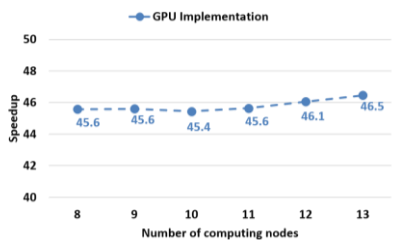


Fig. 7. Scalability analysis for the fixed-workload model.



Nodes	8	9	10	11	12	13
Size (Radius/Unknowns)	8.35/362K	8.5/375K	8.7/394K	8.9/413K	9.05/427K	9.15/439K

Fig. 8. Speed-up analysis for increasing number of nodes along with problem size increases.

V. CONCLUSION

In this paper, MLFMA for homogeneous dielectric objects has been implemented using GPU clusters. Our 13-node GPU cluster is able to solve 426k unknowns utilizing the available on-board GPU memory. It demonstrates that the GPU implementation is much faster than CPU implementation while keeping a same degree of accuracy.

REFERENCES

- [1] O. Ergul and L. Gurel, "Efficient parallelization of the multilevel fast multipole algorithm for the solution of large-scale scattering problems," *IEEE Trans. Antennas Propag.*, vol. 56, no. 8, pp. 2335-2345, August 2008.
- [2] N. Tran and O. Kilic, "Parallel implementations of multilevel fast multipole algorithm on graphical processing unit cluster for large-scale electromagnetics objects," *ACES Express Journal*, vol. 1, no. 4, April 2016.
- [3] R. Coifman, V. Rokhlin, and S. Wandzura, "The fast multipole method for the wave equation: A pedestrian prescription," *IEEE Antennas Propagat. Mag.*, vol. 35, no. 3, pp. 7-12, June 1993.
- [4] H. Samet, *An Overview of Quadtrees, Octrees, and Related Hierarchical Data Structures*. NATO ASI Series, vol. F40, Springer-Verlag Berlin Heidelberg, 1988.
- [5] S. M. Rao, D. R. Wilton, and A. W. Glisson, "Electromagnetic scattering by surfaces of arbitrary shape," *IEEE Trans. Antennas Propag.*, vol. AP-30, no. 3, pp. 409-418, May 1982.
- [6] J.-Y. Li and L.-W. Li, "Characterizing scattering by 3-D arbitrarily shaped homogeneous dielectric objects using fast multipole method," *IEEE Antennas and Wireless Propagation Letters*, vol. 3, 2004.
- [7] Q. M. Nguyen, V. Dang, O. Kilic, and E. El-Araby, "Parallelizing fast multipole method for large-scale electromagnetic problems using GPU clusters," *Antennas and Wireless Propagation Letters, IEEE*, vol. 12, pp. 868-871, 2013.
- [8] V. Dang, Q. Nguyen, and O. Kilic, "Fast multipole method for large-scale electromagnetic scattering problems on GPU cluster and FPGA-accelerated platforms," *Applied Computational Electromagnetics Society Journal*, vol. 28, no. 12, 2013.
- [9] V. Dang, Q. M. Nguyen, and O. Kilic, "GPU cluster implementation of FMM-FFT for large-scale electromagnetic problems," *IEEE Antennas and Wireless Propagation Letters*, vol. 13, 2014.

A Substrate Integrated Waveguide Based Antipodal Linear Tapered Slot Antenna for 60 GHz Wireless Communications

Nishesh Tiwari and Thipparaju R. Rao

Department of Telecommunication Engineering
SRM University, Chennai-603203, India
nitizaz@gmail.com, ramaraot@outlook.com

Abstract — Antipodal linear tapered slot antenna (ALTSA) for 60 GHz communications is presented in this paper. To obtain a high gain, dielectric loading in addition to the corrugation structure is applied to the ALTSA. The use of substrate integrated waveguide (SIW) technology allows a highly efficient, compact and low cost planar design. The antenna is designed and simulated in an electromagnetic field simulation tool. To validate the proposed design, a prototype has been fabricated and measured. The simulated results agree well with the measured values, which validates the proposed design. The radiation efficiency is observed to be 92%. The antenna has a gain of 18.7 ± 0.5 dBi. The return loss is better than 10 dB over the 60 GHz band (57 GHz – 64 GHz).

Index Terms — Antipodal linear tapered slot antenna, dielectric loading, high gain, substrate integrated waveguide, 60 GHz.

I. INTRODUCTION

The ever-growing demand of high speed communication has made the unlicensed 60 GHz band (57 GHz–64 GHz) a smart option for wireless communication allowing transfer of uncompressed data, voice and video at the speed of multi gigabit per second (multi-Gbps) [1]. At millimeter wave frequency band, the losses in the planar microstrip circuit is high. Therefore, this requires more efficient technology like the substrate integrated waveguide (SIW) to be used, which has positive traits of traditional rectangular waveguide such as low loss, high quality factor, complete shielding and capability of handling high power along with the advantage of low cost and planar circuit design [2]. 60 GHz band also suffers from attenuation due to atmospheric absorption. This requires the use of high gain antennas to negate the losses. Tapered slot antennas (TSA) are famous for their high gain and wide bandwidth [3]. TSA with corrugation structure have been used for reducing the width of the antenna while minimizing any significant degradation in

radiation pattern [3]. In [4], Shrivastava et al. have designed corrugated antipodal linear tapered slot antenna (ALTSA) with rectangular corrugation for 60 GHz band having the gain of 16 dBi at 60 GHz. Corrugation also increases gain and reduces side lobe level. Further, dielectric loading is also known for enhancement of antenna gain. By placing the dielectric slab in front of the antenna its gain can be increased. The dielectric slab in this case acts as a guiding structure [5] and enhances the gain of antenna. In [5], Ghassemi et al. have developed a high gain ALTSA array with SIW horn structure as the feed. Rectangular dielectric loading has been used to increase the gain of a non-corrugated ALTSA. In [5], the gain of single ALTSA is 14.25 dBi at 84 GHz and 1x4 ALTSA array is 19 ± 1 dBi. In [6], Wang et al. have applied rectangle shaped dielectric loading structure to a planar SIW horn antenna and achieved a gain of 9.7 dBi at 27 GHz. In [7], Mohamed et al. have presented an ALTSA with diamond slot dielectric loading structure. The antenna has a gain of 16.2 dBi with a wide impedance bandwidth. In [8], Ramesh et al. have designed an exponentially tapered slot antenna (ETSA) with elliptical dielectric loading structure, which has a gain of 11.4 dBi at 60 GHz.

In this paper, instead of conventional elliptical shape, a rectangle with semicircular top shaped dielectric structure is used on a corrugated ALTSA to obtain a high gain antenna in the 60 GHz band. The antenna is designed and simulated in Ansys HFSS software.

II. ANTENNA DESIGN

The antenna is designed on Rogers RT/Duroid 5880 substrate which has dielectric constant of 2.2, loss tangent of 0.0009 and thickness of 0.254 mm. For proper design of SIW, the diameter of via holes and the space between the vias should be chosen as per (1) and (2) respectively:

$$D_{via} < \frac{\lambda_g}{5}, \quad (1)$$

$$S \leq 2D_{via}, \quad (2)$$

where λ_g is the guided wavelength, D_{via} is the diameter of the via and S is the space between the vias. The

effective width of the waveguide is given by (3) [2]:

$$W_{eff} = W_{siw} - 1.08 \frac{D_{via}^2}{S} + 0.1 \frac{D_{via}^2}{W_{siw}}, \quad (3)$$

where W_{eff} is the effective width, W_{siw} is the width of the SIW. The performance of TSA is sensitive to the thickness t and the dielectric constant ϵ_r . Hence, a factor $f_{substrate}$ is defined for efficient performance of TSA as $f_{substrate} = t(\sqrt{\epsilon_r} - 1)/\lambda_0$ [3]. For good performance of tapered slot antenna, the substrate thickness should satisfy $0.005 \leq f_{substrate} \leq 0.03$. In this design we have chosen the substrate thickness of 0.254 mm such that $f_{substrate}$ is 0.024. ALTSA is generally designed with trial and error method. The width of the ALTSA is kept greater than 2λ [5]. The length of the flares is increased gradually until the optimum gain is achieved. Generally, the length varies from $3\lambda - 8\lambda$ to achieve the optimum gain. In this work, the optimum gain is observed when the length of the flares is 5λ . Firstly, the plain ALTSA is designed. Then corrugation is applied to the outer edges of the flares. Finally, a dielectric slab is added on top of the corrugated ALTSA to form the dielectric loaded ALTSA. The plain ALTSA (ALTSA-P), corrugated ALTSA (ALTSA-C) and corrugated ALTSA with dielectric loading (ALTSA-DL) are designed and simulated. Figure 1 shows the schematic of ALTSA-DL where $L1 = 11.95$ mm, $L2 = 10.5$ mm, $L3 = 25$ mm, $L4 = 15$ mm, $L5 = 0.4$ mm, $W1 = 1.59$ mm, $W2 = 2.69$ mm, $W3 = 10.1$ mm, $W4 = W5 = 0.2$ mm, $r = 5.05$ mm, $V = 0.78$ mm, $D_{via} = 0.4$ mm, $S = 0.7$ mm.

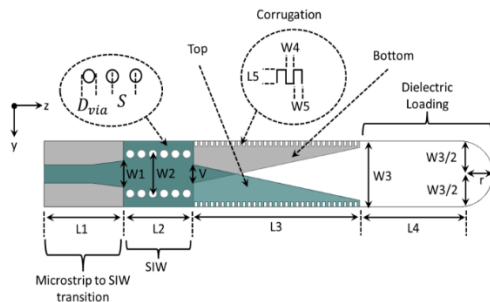


Fig. 1. ALTSA-DL schematic.

The structure of the dielectric load used in antenna has an impact on its gain. In this work, instead of a conventional elliptical dielectric loading structure, a rectangle with semi-circular top shaped design for dielectric loading is proposed. During simulation it is observed that rectangle with semicircular top shaped dielectric loading gives higher gain than conventional elliptical dielectric loading structure. The maximum difference in gain is observed to be around 0.76 dBi.

III. SIMULATION AND MEASUREMENT

Figure 2 shows the E-field distribution. The simulated gain and return loss of ALTSA are shown in Fig. 3. It is observed that return loss for ALTSA-P,

ALTSA-C and ALTSA-DL are all better than 10 dB in the 60 GHz band (57-64 GHz). Also, it is observed that the return loss changes as corrugation and dielectric loading structure is added to the antenna. At 60 GHz, the ALTSA-DL has return loss better than 23 dB. Similarly, from Fig. 3 it is also observed that the gain of ALTSA-P, ALTSA-C and ALTSA-DL is 14.4 ± 0.3 dBi, 17.1 ± 0.3 dBi and 18.8 ± 0.6 dBi respectively. The simulated E-plane radiation pattern is shown in Fig. 4. In the E-plane the 3-dB beamwidth of ALTSA-P, ALTSA-C and ALTSA-DL is observed to be 22.6° , 19.5° and 17.5° respectively. Also, the side lobe level of ALTSA-P, ALTSA-C and ALTSA-DL in E-plane is observed to be at -13 dB, -15 dB and -17 dB respectively. Similarly, the cross polarization level of ALTSA-P, ALTSA-C and ALTSA-DL is observed to be better than 14 dB, 21 dB and 22 dB respectively.

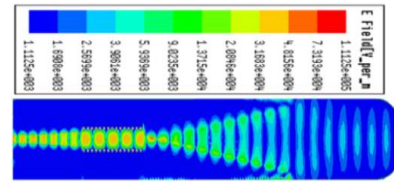


Fig. 2. E-field distribution in ALTSA-DL.

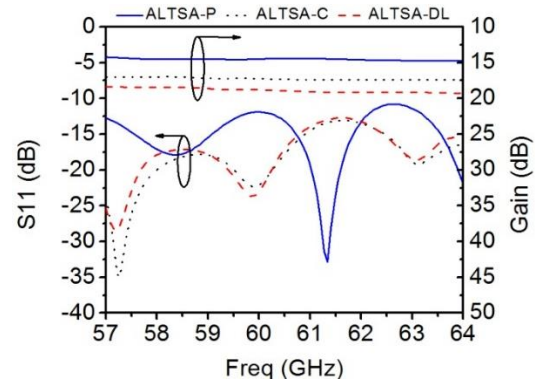


Fig. 3. Simulated return loss and gain.

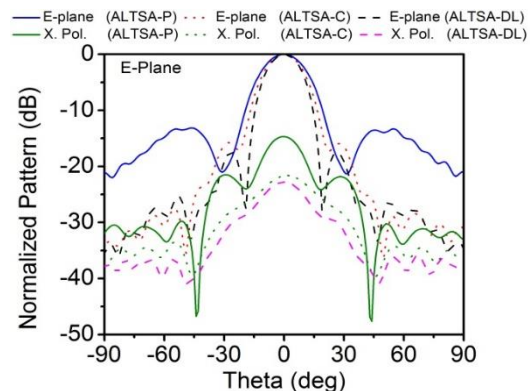


Fig. 4. Simulated E-plane radiation pattern at 60 GHz.

The simulated H-plane radiation pattern is shown in Fig. 5. The 3-dB beamwidth in the H-plane of ATLSA-P, AL TSA-C and AL TSA-DL is observed to be 29.5°, 33.1° and 25.2° respectively. Further, the side lobe level of AL TSA-P, AL TSA-C and AL TSA-DL in H-plane is observed to be -13 dB, -12 dB and -15dB respectively. Also, the cross polarization level of AL TSA-P, AL TSA-C and AL TSA-DL is seen to be better than 14 dB, 21 dB and 22 dB respectively. It is noted that, though with corrugation the E-plane beamwidth decreases but the beamwidth increases in H-plane. Overall it is found that AL TSA-DL has the narrowest beamwidth, lowest side lobe level and better cross polarization in both E- and H-planes. Therefore AL TSA-DL is found to have the best performance. Hence, AL TSA-DL is fabricated and its performance parameters are measured to validate the design.

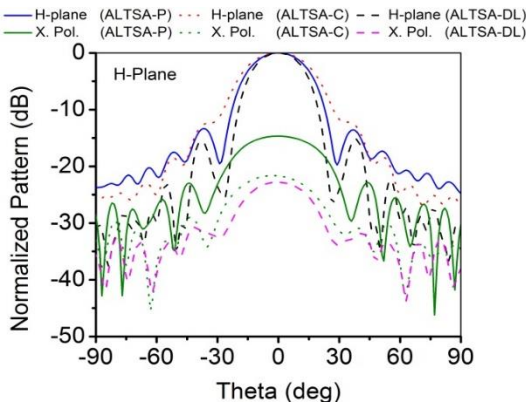


Fig. 5. Simulated H-plane radiation pattern at 60 GHz.

Figure 6 shows the fabricated AL TSA-DL prototype. The dimension of AL TSA-DL is 67.5 mm x 10.1 mm. It is compact in size and light weight. It is fabricated using the low cost printed circuit board (PCB) technology. The S11 parameters and gain of AL TSA-DL are measured utilizing MVNA-8-350 with probe station. The radiation pattern measurement has been performed in a far-field anechoic chamber.

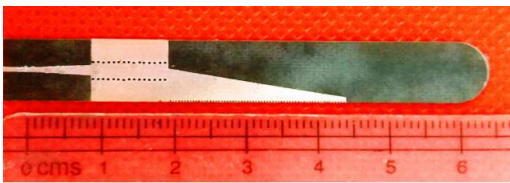


Fig. 6. Fabricated AL TSA-DL.

Figure 7 shows the measured gain and return loss of the AL TSA-DL. From Fig. 7, it is observed that measured gain of AL TSA-DL is 18.7 ± 0.5 dB over the entire 60 GHz band (57-64 GHz). The antenna gain is almost flat over the entire bandwidth. Similarly, measured return loss

is observed to be better than 12 dB over the 60 GHz band. At 60 GHz, return loss is better than 22 dB. The discrepancy observed in the measured return loss with slight frequency shift can be attributed to the fabrication tolerances. Figure 8 shows the measured E-plane radiation pattern of AL TSA-DL at 60 GHz. The measured 3-dB beamwidth of AL TSA-DL in E-plane is 17° and the side lobe level is at -17 dB, which is similar to the values obtained from simulation. Similarly, Fig. 9 shows the measured H-plane radiation pattern of AL TSA-DL at 60 GHz. The measured 3-dB beamwidth of AL TSA-DL in H-plane is observed to be 22.7° and the side lobe level is at -15.7 dB. Further, it is seen that the simulated and measured radiation patterns are in good agreement in both E-plane and H-plane. Also, the radiation efficiency is observed to be 92%.

Table 1 lists the comparison with other SIW based antennas having different dielectric loading structures such as rectangle in [6], elliptical in [8] etc. It is observed that though the proposed antenna has less impedance bandwidth as compared to [7], its gain is better as compared to other antennas. Further, its impedance bandwidth covers 57-64 GHz, which is adequate for multi-Gbps communication at 60 GHz.

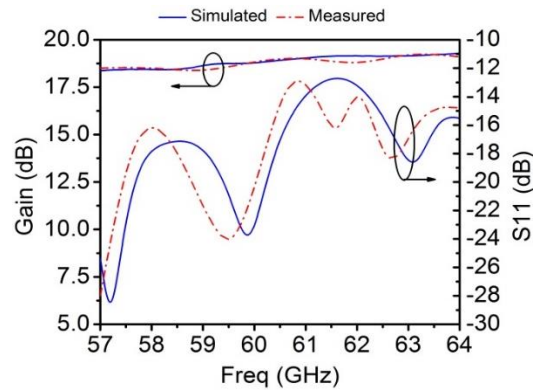


Fig. 7. Simulated and measured return loss and gain of AL TSA-DL.

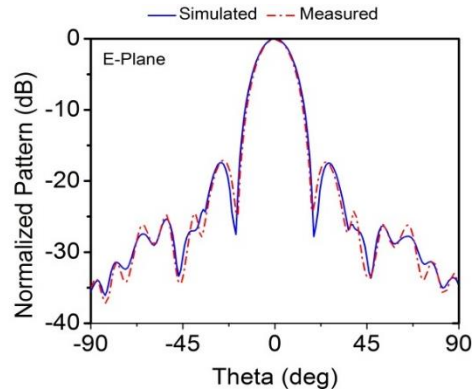


Fig. 8. Simulated and measured E-plane radiation pattern of AL TSA-DL at 60 GHz.

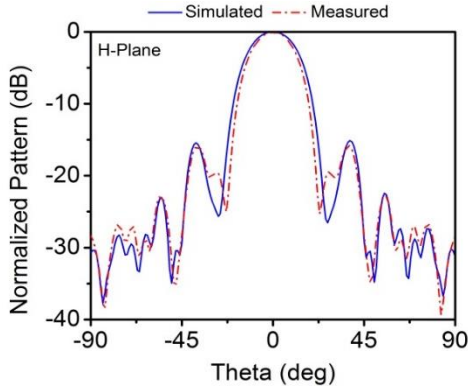


Fig. 9. Simulated and measured H-plane radiation pattern of ALTSA-DL at 60 GHz.

Table 1: Comparison with other antennas

Parameter	[6]	[7]	[8]	This Work
Antenna	Horn	ALTSA	ETSA	ALTSA
Dielectric loading structure	Rect.	Diamond slot	Ellip.	Rect. with semicircular top
Gain (dBi)	9.7	16.2	11.4	18.8
Impedance bandwidth	5.5%	33.3%	5.5%	11.6%
Operation frequency (GHz)	27	60	60	60

IV. CONCLUSION

A high gain ALTSA with dielectric loading is presented in this paper. The antenna has high gain, compact size, light weight, ease of fabrication using PCB technology and it is also fit for mass production. Hence, the proposed antenna is suitable for high speed communication in 60 GHz band.

ACKNOWLEDGMENT

Authors are very much obliged to ISRO, Government of India, for their assistance provided for the execution of this research work.

REFERENCES

- [1] P. Smulders, "Exploiting the 60 GHz band for local wireless multimedia access: Prospects and future directions," *IEEE Communication Magazine*, vol. 40, pp. 140-147, 2002.
- [2] M. Bozzi, A. Georgiadis, and K. Wu, "Review of substrate-integrated waveguide circuits and antennas," *IET Microwaves, Antennas & Propagation*, vol. 5, pp. 909-920, 2011.
- [3] T. Djerafi and K. Wu, "Corrugated substrate integrated waveguide antipodal linearly tapered slot antenna array fed by quasi-triangular power divider," *PIER C*, vol. 26, pp. 139-151, 2012.
- [4] P. Shrivastava, D. Chandra, N. Tiwari, and T. R. Rao, "Investigations on corrugation issues in SIW based antipodal linear tapered slot antenna for wireless networks at 60 GHz," *ACES Journal*, vol. 28, pp. 960-967, 2013.
- [5] N. Ghassemi and K. Wu, "Planar high-gain dielectric-loaded antipodal linearly tapered slot antenna for E- and W-band gigabyte point-to-point wireless services," *IEEE Transactions on Antennas and Propagation*, vol. 61, pp. 1747-1755, 2013.
- [6] H. Wang, D. G. Fang, B. Zhang, and W. Q. Che, "Dielectric loaded substrate integrated waveguide (SIW) H-plane horn antennas," *IEEE Transactions on Antennas and Propagation*, vol. 58, pp. 640-647, 2010.
- [7] I. Mohamed and A. Sebak, "Dielectric loaded antipodal linearly tapered slot antenna for 60 GHz applications," *Global Symposium on Millimeter Waves*, pp. 1-2, 2015.
- [8] S. Ramesh and T. R. Rao, "Planar high gain dielectric loaded exponentially tapered slot antenna for millimeter wave wireless communications," *Wireless Personal Communications*, vol. 84, pp. 3179-3192, 2015.

Installed Antenna Performance in Airborne Radomes of Different Profiles

Ana Vukovic, Phillip Sewell, Xuesong Meng, and Trevor M. Benson

George Green Institute for Electromagnetics Research, Department of Electrical and Electronic Engineering
University of Nottingham, Nottingham, NG7 2RD, UK
ana.vukovic@nottingham.ac.uk, xuesong.meng@nottingham.ac.uk, trevor.benson@nottingham.ac.uk,
phillip.sewell@nottingham.ac.uk

Abstract — In this paper, broadband interactions between an antenna and a radome are modelled using a full wave numerical solver. By accurately describing both the antenna and the radome geometry with a single numerical method, a comprehensive prediction of the performance of the coupled antenna and radome installation is provided. The paper compares how different airborne dielectric radome profiles affect the antenna performance, predicting effects not seen in uncoupled simulations.

Index Terms — Airborne radome, installed antenna, unstructured transmission line modelling method.

I. INTRODUCTION

Airborne radomes are weatherproof enclosures that protect antennas from the physical environment but are intended to have minimal impact on antenna performance. In practice, the aerodynamic requirements on a radome's profile compromises their benign nature for installed antenna performance; this typically manifests itself as an increase in the sidelobe level of the antenna radiation pattern and as a boresight error [1]. This is particularly true in cases where the antenna is installed close to the radome surface. In such scenarios, a better understanding of antenna-radome interactions is necessary for accurate predictions of deployed antenna performance.

Over the last decade, rapid progress in computational power and advances in distributed processing, mean that a number of numerical techniques are ever more capable of tackling larger and complex problems. Notwithstanding the advances in modelling capability, it is notable that the analysis of the electromagnetic interactions between antennas and radomes is still performed in a “decoupled” fashion, even for moderately sized problems, due to the multiscale nature of the antenna and the radome geometry [1, 2]. One common approach is to replace the intricate detail of the antenna geometry by a 3D surface of equivalent electric and magnetic currents [1]. Alternatively, the radiating fields from the antenna are computed without the radome and subsequent evaluation of the effect of the radome on the radiation pattern is performed using these fields as an excitation [1, 2]. In

both approaches, decoupling the antenna from the radome means that their mutual interactions are not fully taken into account in the design and simulation cycle. It is immediately obvious that, in order to take full account of these interactions, a flexible, accurate and efficient broadband solver that can efficiently deal with the multiscale features and complex geometries of the problem is required.

In this paper we report on the application of the numerical time-domain Transmission Line Modelling (TLM) method to the fully-coupled modelling of the moderate size problem posed by radome-antenna interactions. Both the antenna and the radome are discretized within a single numerical method based upon an unstructured tetrahedral mesh, referred to as the Unstructured TLM (UTLM) method. The TLM method exploits the analogy between solutions of the 3D Maxwell's equations for electromagnetic fields and voltages and currents on an interconnected network of transmission lines to identify an explicit time stepping algorithm for the electromagnetic fields. Development of the TLM method for use with unstructured tetrahedral meshes was first reported in [3, 4] and has since been fully characterized. Unlike the finite difference and finite element time domain (FDTD, FETD) methods, the UTLM method is unconditionally stable, with stability strictly provable a priori on cell by cell basis. Late time instability is never observed and the explicit nature of the algorithm is highly efficient, without for example, introducing approaches such as mass lumping. TLM time stepping algorithms exhibit a high degree of concurrency, and hence, parallelize well on many-core processors systems. Use of tetrahedral meshes eliminates the numerical noise due to the staircase approximations to geometry typically found in the simplistic Cartesian TLM and FDTD methods. Moreover, smoother representations of curved geometrical boundaries and the inherent availability of graded meshes that permit efficient discretization of subwavelength features in large computational domains are also advantageous. The latter can be facilitated by either using a purely tetrahedral mesh, or more practically, by hybridizing

computationally efficient cubic grids and tetrahedral meshes, e.g., [5].

In this paper, antenna-radome interactions are modelled in a fully coupled manner using the UTLM method. A single broadband Vivaldi antenna enclosed in a monolithic dielectric radome of moderate size is selected as the test case. Besides the discretization, the UTLM method makes no other approximation and as long as a sufficiently fine mesh is used to discretize the whole problem, we can be assured that all physical interactions are accounted for. The open end of the dielectric radome is mounted on a perfectly conducting surface consistent with practical airborne installations. In order to separate the effect of this mounting plate and the radome's profile, the effect of the presence of just this mounting plate on the antenna's performance is investigated before the radome itself is added to the model. Spherical, spherically blunted cone and two types of superspheroidal radomes are considered, and antenna-radome interactions are assessed in terms of the return loss, S_{11} , and the radiation patterns of the installed antenna. The paper is structured as follows. In the next section the antenna geometry mounted on just the conducting plate is described and modelled. Section III then assesses how different radome profiles affect the antenna's performance, and Section IV summarizes the main conclusions of the paper.

II. ANTENNA ON THE RADOME MOUNTING PLATE

In this section, the performance of the Vivaldi antenna described in [6] mounted on a moderate size conducting plate is described. The slot line is printed on a substrate of dielectric constant $\epsilon_{rs}=3$ and is flared to provide a smooth impedance transition between the coaxial feed and free space. The half width of the slot line varies with distance as $w(z) = 0.25e^{0.0797z}$ reaching 20 mm at the wider end. A balun is realized as a void in the flared metallic region of radius 2.5 mm. The height, width and thickness of the dielectric substrate are 55 mm, 40 mm and 1.5 mm respectively. The perfectly conducting plate is cylindrical with radius 2 m and thickness 7 mm. The coaxial feed, designed to have a characteristic impedance of 50 Ω , has inner and outer radius of 1 mm and 3.495 mm, and dielectric constant of $\epsilon_{rc} = 2.25$. The problem space is surrounded by a fictitious surface of dimensions 4.8 m x 4.6 m x 6.2 m to both terminate the space with a free space radiation boundary condition and on which to capture the radiation fields. The antenna is excited with the TEM mode of the coaxial feed modulated by a time envelope to provide a center frequency of 3.2 GHz [6] and a bandwidth spanning 1.5 to 4.5 GHz.

An example of the antenna and radome mounting plate geometry is shown in Fig. 1 and the complete geometry with a radome is shown in the inset of the Fig.

1. The whole problem is meshed with a 5 mm cubic mesh to sample the free space region [6] in conjunction with a high quality tetrahedral mesh to capture the detailed geometry. Specifically, the surfaces of, and the space around, the antenna and feed cable shown in Fig. 1, are sampled by triangular and tetrahedral cells characterized by the figure of merit $Q=2$. (Cell Q is defined as the ratio between the circumradius to the minimum edge length of the cell and generally values less than 5 correspond to nicely shaped cells yielding good spatial sampling [7]).

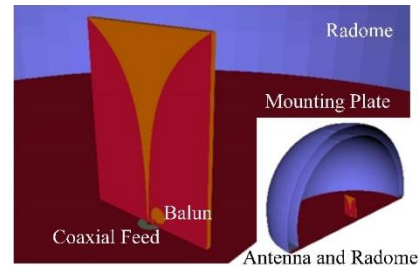


Fig. 1. Antenna on the radome mounting plate and antenna inside a radome in the inset of the figure.

Figure 2 presents S_{11} parameter for the antenna mounted on just the perfectly conducting plate. To assess the impact of mesh dispersion errors and sensitivity to the meshing in general, the simulation was also repeated using the mesh obtained when a *ghost* spherical half-wave dielectric radome of thickness of 24.2 mm, but of relative permittivity set to $\epsilon_r=1$, is present. Physically, the radome is not electromagnetically present, but its geometry is still imprinted on the mesh. Finally, a spherical half-wave dielectric radome of permittivity $\epsilon_r=4.2$ and wall thickness of 24.4 mm, designed to operate at 3 GHz was introduced. Figure 2 shows that there is no difference between the performance of the antenna on the just mounting plate, and with the *ghost* radome in place over the operating range, indicating no discernable sensitivity to the meshing. Moreover, this result agrees very well with that already reported in [6]. However, when for the first time, a fully coupled simulation is performed in the presence of the dielectric radome, it can be seen that S_{11} deteriorates over the operating range due to reflections from the radome. For reference, the computations simulated a total of 0.02 μs using a time step of $\Delta t=0.01ps$ on 25 processor cores of a commodity cluster and required ~ 5.5 h to complete.

Figures 3 (a, b) compares the radiation patterns in the H- and E-plane for all three cases. Figure 3 (a) also shows the coordinate planes and the azimuthal H-plane denoted by angle ϕ and the elevation E-plane denoted by angle θ . Figure 3 shows that the radiation patterns for the antenna just on the mounting plate and with the *ghost* radome are identical, whereas the presence of the dielectric spherical radome causes stronger rippling in

the main beam of the H-plane pattern ($\phi=270$ deg) and increased radiation in the sidelobe ($\theta=90$ deg), as shown in Fig. 3 (a). The E-plane radiation pattern of the dielectric spherical radome shows slightly lower directivity compared to the antenna just on the mounting plate.

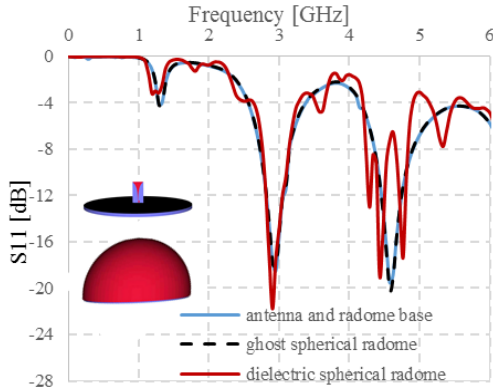


Fig. 2. S_{11} for the antenna on the mounting plate, with the *ghost* spherical radome and the dielectric spherical radome with $\epsilon_r=4.2$.

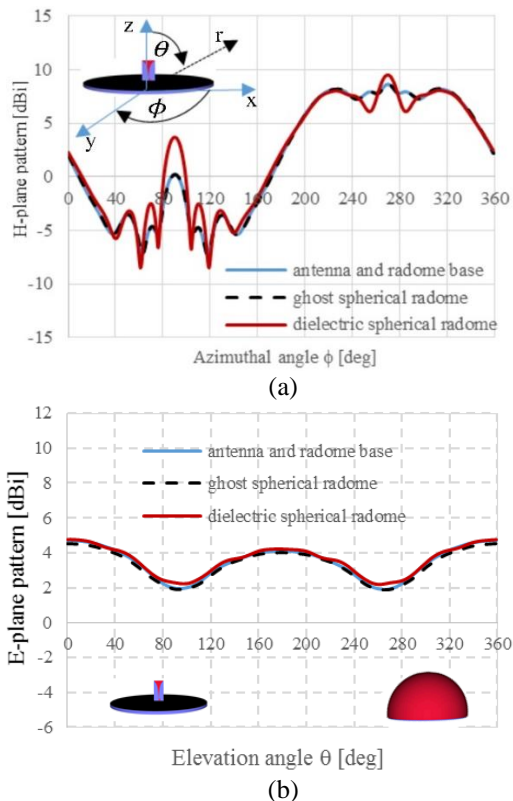


Fig. 3. (a) H-plane pattern and (b) E-plane radiation pattern for antenna on the radome base, with *ghost* spherical radome and the dielectric spherical radome.

III. IMPACT OF DIFFERENT RADOME PROFILES ON ANTENNA PERFORMANCE

In this section, the performance of the Vivaldi antenna installed in several different radomes is analyzed and compared with the case of antenna mounted on the radome base, i.e., without a radome. Illustrative aerodynamic radome profiles are chosen, namely, a spherically blunted cone and two superspheroidal profiles. In all cases, the radome's base radius and length are fixed to be $R=2$ m and $L=2.2$ m respectively. In all cases, the half-wave monolithic radome is made of a glass composite of thickness 24.4 mm and dielectric constant $\epsilon_r=4.2$, which is designed to operate at 3 GHz. Radome losses are neglected. The cone profile radome is blunted by a sphere of radius 0.1 m. The superspheroidal radomes are described by the equation $x^2 + y^2 = \left(\frac{2R}{L}\right)^2 (L^p - z^p)^{2/p}$, where the coordinate z is defined along the axis of the radome, and parameter p defines the particular profile; $p=1.449$ and $p=1.161$ give the ogive and superspheroidal profiles of [2] respectively. All simulations were performed with the same meshing and run time parameters given in Section II.

Figure 4 assesses S_{11} in the operating range for the antenna installed in three different airborne radomes. The radome profiles are also given in Fig. 4. Figure 4 shows that reflections from the superspheroidal radomes tend to shift the operating frequency of the antenna and to narrow the antenna's passband. The spherically blunted cone has the least impact on S_{11} in the passband and gives the most similar behavior to the antenna performance without a radome.

Figures 5 (a, b) compares the antenna radiation patterns for the H-plane and E-plane for each radome. Figure 5 (a) shows that the superspheroid with $p=1.161$ causes the highest deterioration in the main lobe of the H-plane radiation pattern ($\phi=270$ deg). The ogive radome ($p=1.449$) has reduced the directivity of the main beam of antenna ($\phi=270$ deg). The spherically blunted radome has the radiation pattern most similar to the antenna with no radome. All radomes cause the slight increase in the side lobe ($\phi=90$ deg). Figure 5 (b) shows that in the E-plane, the superspheroid with $p=1.161$ has significantly increased the directivity of antenna whilst the ogive radome ($p=1.449$) has decreased the directivity in the E-plane. Again, the spherically blunted radome has the E-plane pattern most similar to the antenna with no radome.

Our analysis of the effect that different superspheroidal radome profiles have on the radiation pattern of the antenna are very different from those in [2] that reported only very minor differences in sidelobes of the antenna radiation. This is, we believe, due to the "decoupled" approach employed in [2].

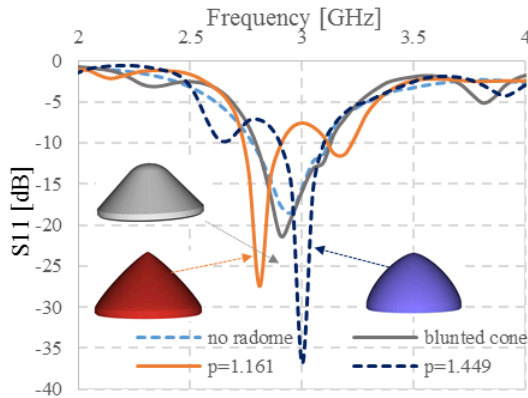


Fig. 4. Comparison of antenna S_{11} parameter in the presence of different radome profiles.

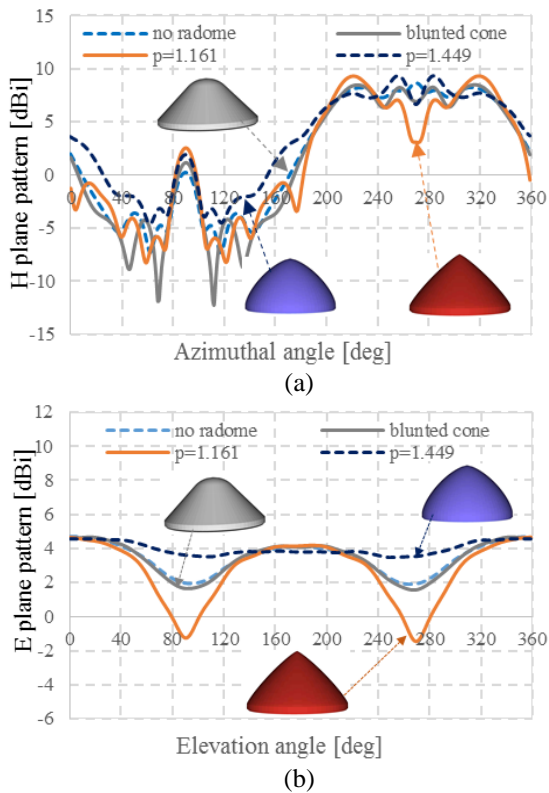


Fig. 5. Comparison of the antenna radiation pattern in the presence of different radomes for: (a) H-plane and (b) E-plane.

IV. CONCLUSION

The paper analyses broadband interactions between antennas installed in airborne radomes in a fully coupled manner by directly sampling both the antenna and the radome geometry using a single numerical method. In order to isolate the effect of the radome, the antenna's performance is first modelled in the presence of just the radome base. Two different superspheroidal radomes

and the spherically blunted cone are then introduced and their impact on the antenna's performance assessed. The paper shows that a spherically blunted cone has the least influence on antenna's performance and that superspheroids can significantly change the antennas performance and need to be designed with care.

ACKNOWLEDGMENT

The authors wish to thank Dr. S. Earl and Prof. C. Jones of BAE SYSTEMS for many valuable discussions.

REFERENCES

- [1] R. U. Nair and R. M. Jha, "Electromagnetic design and performance analysis of airborne radomes: Trends and perspectives," *IEEE Antennas and Prop. Magazine*, vol. 56, pp. 276-298, 2014.
- [2] W.-J. Zhao, L.-W. Li, and Y.-B. Gan, "Efficient analysis of antenna radiation in the presence of airborne dielectric radomes of arbitrary shape," *IEEE Trans. Antennas and Prop.*, vol. 53, pp. 442-448, 2005.
- [3] P. Sewell, T. M. Benson, C. Christopoulos, D. W. P. Thomas, A. Vukovic, and J. G. Wykes, "Transmission line modeling (TLM) based upon unstructured tetrahedral meshes," *IEEE Trans. Microwave Theory and Tech.*, vol. 53, pp. 1919-1928, 2005.
- [4] P. Sewell, T. M. Benson, C. Christopoulos, D. W. P. Thomas, A. Vukovic, and J. G. Wykes, "Implicit element clustering for tetrahedral transmission-line modeling (TLM)," *IEEE Trans. Microw. Theory Tech.*, vol. 57, no. 6, pp. 2005-2014, June 2009.
- [5] P. Sewell, J. G. Wykes, T. M. Benson, C. Christopoulos, D. W. P. Thomas, and A. Vukovic, "Multi-grid interface in computational electromagnetics," *Electron. Lett.*, vol. 40, pp. 162-163, 2004.
- [6] A. E. Yilmaz, Z. Lou, E. Michielssen, and J. M. Jin, "A single boundary implicit and FFT-accelerated time-domain finite element-boundary integral solver," *IEEE Trans. Antennas and Propagat.*, vol. 55, pp. 1382-1397, 2007.
- [7] J. Shewchuk, Lecture notes on Delaunay Mesh Generation. <https://people.eecs.berkeley.edu/~jrs/meshpapers/delnotes.pdf>

A Compact Fractal Monopole Antenna with Defected Ground Structure for Wideband Communication

Ankan Bhattacharya^{1*}, Bappaditya Roy¹, Santosh K. Chowdhury²,
and Anup K. Bhattacharjee¹

¹ Department of Electronics and Communication Engineering
National Institute of Technology, Durgapur-713209, India
*bhattacharya.ankan1987@gmail.com

² Department of Electronics and Telecommunication Engineering
Jadavpur University, Kolkata-700032, India

Abstract — A compact fractal monopole antenna with defected ground structure has been investigated in this paper. A wide bandwidth of 3.13 GHz (3.42 GHz to 6.55 GHz) has been obtained, which covers the IEEE 802.11 WLAN bands (5.2 GHz and 5.8 GHz) and WiMAX bands (3.5 GHz and 5.5 GHz). The dimension of the structure is 14.50 X 27.25 mm² covering an area of only 395.125 mm². The realized antenna gain is ≥ 2 dBi at the frequencies of interest. The compactness of the proposed structure and the simplicity of design makes it easy to be fabricated and incorporated in devices suited for wireless communication purpose.

Index Terms — Defected ground structure, fractal geometry, monopole antenna, wideband communication

I. INTRODUCTION

With the advent of portable mobile devices, there is a huge need for compact, low-profile patch antennas for space conservation and also for wideband communication purpose. From literature survey, it has been found that though several wideband antennas have been proposed for wideband applications particularly for WLAN and WiMAX microwave frequency bands; there still exists an issue regarding compactness in shape and size and also in realized gain of the antennas. A dual band antenna with fractal based ground plane has been proposed in [1]. The dimension of the structure is almost equal to 104 X 30 mm². A perturbed Sierpinski carpet antenna with CPW feed for IEEE 802.11 a/b WLAN application has been presented in [2]. The dimension of the antenna is 45 X 67.8 mm². A microstrip line fed printed wide slot antenna has been investigated in [3]. The antenna dimension is 70 X 70 mm². A broadband circularly polarized Spidron fractal slot antenna has been presented in [4]. The dimension of the proposed structure is 40 X 40 mm². A wideband fractal antenna with combination

of fractal geometries has been presented in [5] for WLAN and WiMAX applications. The dimension of the structure is 25 X 66 mm². Similar types of investigations have been studied in [6] and [7], but in each case there arises an issue regarding the compactness of the proposed antenna structure. In this article, a compact fractal monopole antenna with defected ground structure has been investigated. A wide bandwidth of 3.13 GHz (3.42 GHz to 6.55 GHz) has been obtained, which covers the IEEE 802.11 WLAN bands (5.2 GHz and 5.8 GHz) and WiMAX bands (3.5 GHz and 5.5 GHz). The dimension of the structure is 14.50 X 27.25 mm² covering an area of only 395.125 mm². The realized antenna gain at the frequencies of interest are 2.5 dBi, 3.5 dBi, 3.5 dBi and 3.6 dBi at 3.5 GHz, 5.2 GHz, 5.5 GHz and 5.8 GHz respectively.

II. ANTENNA DESIGN

The objective of this work is to design a low-profile antenna, compact in shape and size with standard gain limits for wideband operations. The dimension of the proposed structure is 14.50 X 27.25 mm² covering an area of only 395.125 mm². Repeated square fractal geometry has been applied in design of the patch structure. The width of the feed line has been chosen to match 50 Ω impedance using (1) and (2).

For the proposed design, substrate dielectric constant, $\epsilon_r = 4.3$, substrate height, $h = 1.5$ mm and width of feed line, $Fw = 3.0$ mm:

$$\epsilon_{eff} = \frac{\epsilon_r + 1}{2} + \frac{\epsilon_r - 1}{2} \frac{1}{\sqrt{(1 + 12h/Fw)}}, \quad (1)$$

$$Z_o = \frac{120\pi}{\sqrt{\epsilon_{eff}} \left[\frac{Fw}{h} + 1.393 + 0.667 \ln \left(\frac{Fw}{h} + 1.444 \right) \right]}, \quad (2)$$

where Z_o is the characteristic impedance and ϵ_{eff} is the effective dielectric constant of Substrate.

FR-4 substrate, which is commonly available in the market is used as the substrate for the proposed design.

The thickness of the substrate is kept equal to 1.5 mm. The patch and the ground plane are built of 0.5 mm thick copper plates. The patch and the ground plane is composed of Copper (annealed). The ground plane is not continuous throughout the design. A portion of the ground plane has been etched from the top. Two L-shaped slots have been introduced in the ground plane along with an I-shaped slot in the middle. The dimension of these slots have been chosen after parametric optimization. This type of etched ground structure is known as Defected Ground Structure (DGS) in antenna engineering and research. Incorporation of DGS in antenna design has an effect on frequency response of the antenna, which has been discussed later. Repeated square structures have been used in design of the patch as shown in Fig. 1.

The proposed repeated square fractal carpet geometry used to design the patch structure (Fig. 1.). The proposed antenna has been shown in Fig. 2.

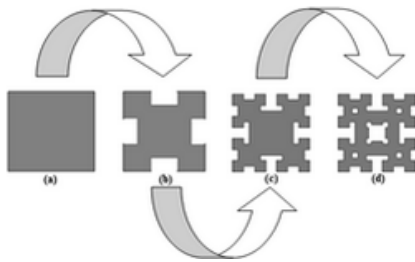


Fig. 1. Proposed fractal carpet geometry: (a) basic geometry, (b) 1st iteration, (c) 2nd iteration, and (d) 3rd iteration.

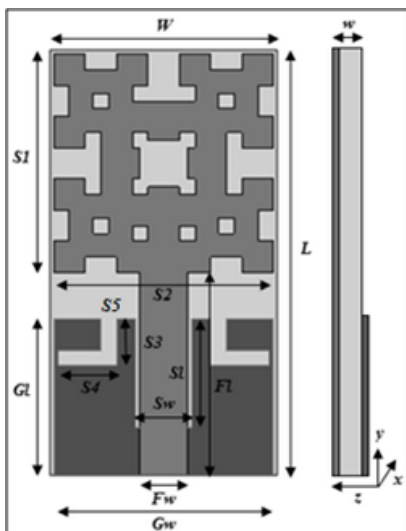


Fig. 2. Proposed fractal antenna with side view.

Genetic Algorithm (GA) has been applied for parametric optimization. The detailed parameter dimensions are provided in Table 1. It may be noted

that, the overall area of proposed structure is only $W \times L = 14.50 \times 27.25 = 395.125 \text{ mm}^2$.

Table 1: Parameter dimensions (in mm)

Parameter	Dimension	Parameter	Dimension
W	14.50	Fw	03.00
L	27.25	Fl	13.00
$S1$	14.00	Gw	14.00
$S2$	14.00	Gl	10.00
$S3$	03.00	Sw	03.50
$S4$	03.75	Sl	07.00
$S5$	01.00	w	02.50

III. RESULTS AND DISCUSSION

The proposed antenna structure with different patch shapes in successive iterative stages has been simulated and the results have been displayed in Fig. 3.

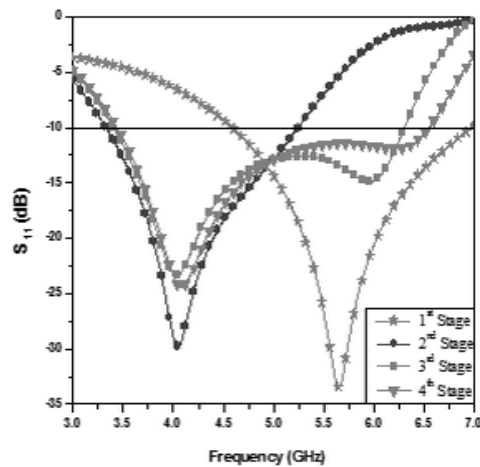


Fig. 3. Return loss of antenna at various iterative stages.

From Fig. 3, it has been observed that the resonant frequency near 5.6 GHz in the 1st stage gradually shifts towards the left near 4.0 GHz in the 2nd iterative stage with gradual interment in bandwidth in the successive stages. A maximum bandwidth of 3.13 GHz (3.42 GHz to 6.55 GHz) has been obtained, which covers the IEEE 802.11 WLAN bands (5.2 GHz and 5.8 GHz) and WiMAX bands (3.5 GHz and 5.5 GHz) in the 4th or final iterative stage.

Defected Ground Structures (DGS) are used now-a-days by antenna researchers to improve the frequency response characteristics of the antenna. A fraction of the propagating energy is stored by the ground plane, which has an effect on overall frequency response of the antenna structure. Figure 4 shows the S_{11} vs. frequency plot for the antenna with and without the presence of DGS.

The proposed structure has been fabricated as shown in Fig. 5. The front view (Fig. 5 (a)) shows the fractal square patch and the 50 Ω feed line. The rear view (Fig.

5 (b)) shows the DGS ground plane. The dimension of the structure is comparable to a “1 Rupee Indian Coin”. The dimension of the structure is 14.50 X 27.25 mm² covering an area of only 395.125 mm². Due to its low-profile structure, the proposed antenna has a very small coverage area and can easily be integrated in compact and low-profile devices supporting wideband operations.

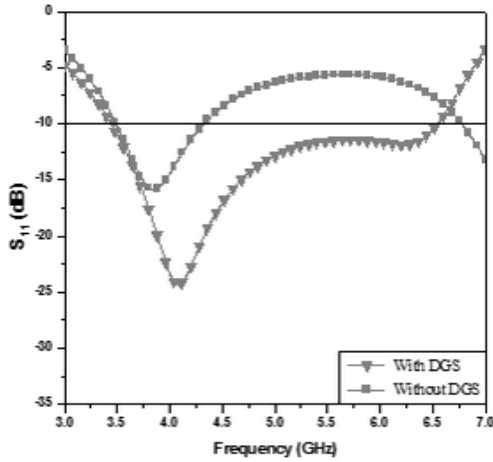


Fig. 4. Return loss of antenna with and without DGS.

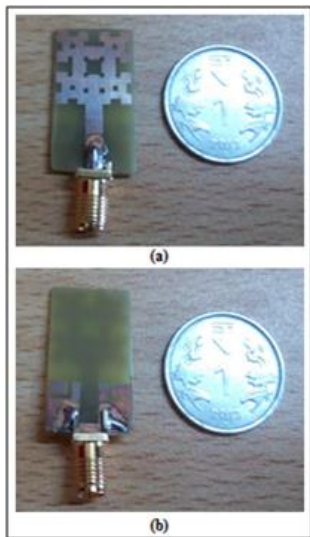


Fig. 5. Fabricated prototype: (a) front view and (b) rear view.

Simulated and measured return losses have been shown in Fig. 6. The results bear a good agreement. Slight discrepancy in result may be due to the effect of soldering. 2D polar plot of the antenna has been shown in Fig. 7. Isolation level between co and cross-polarizations greater than 100 dB has been maintained with almost omni-directional H-plane patterns (Fig. 7.). The simulated and measured antenna gains are plotted in Fig. 8. The realized antenna gain (measured) at the

frequencies of interest are 2.5 dBi, 3.5 dBi, 3.5 dBi and 3.6 dBi at 3.5 GHz, 5.2 GHz, 5.5 GHz and 5.8 GHz respectively; which is quite decent for wideband operation. Figure 9 shows the antenna surface current distribution pattern. It can be observed from that, the current originates from the feed and distributes itself uniformly at the edges of the patch. The resonant modes thereby generated, come closer resulting in a wider bandwidth.

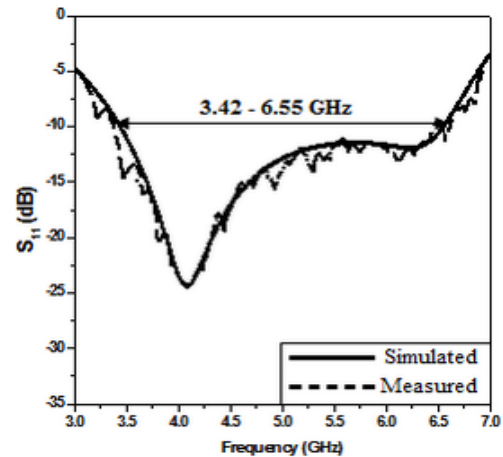


Fig. 6. Simulated and measured return losses.

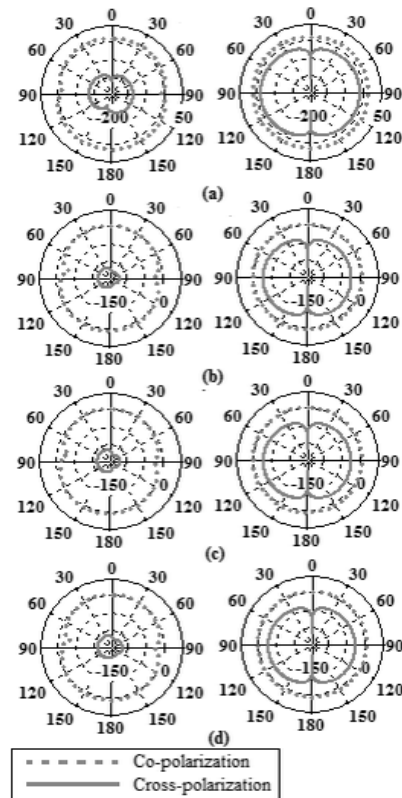


Fig. 7. 2D polar plot of E-plane (left) and H-plane (right) at: (a) 3.5 GHz, (b) 5.2 GHz, (c) 5.5 GHz, and (d) 5.8 GHz.

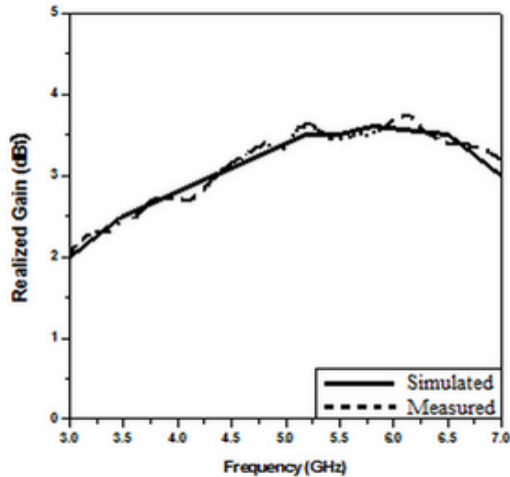


Fig. 8. Realized gain of proposed antenna.

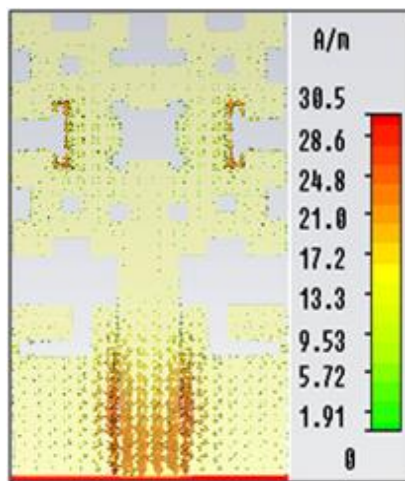


Fig. 9. Antenna surface current distribution pattern.

IV. CONCLUSION

A compact fractal monopole antenna with defected ground structure has been investigated in this paper. A wide bandwidth of 3.13 GHz (3.42 GHz to 6.55 GHz) has been obtained, which covers the IEEE 802.11 WLAN bands (5.2 GHz and 5.8 GHz) and WiMAX bands (3.5 GHz and 5.5 GHz). The dimension of the structure is 14.50 X 27.25 mm² covering an area of

only 395.125 mm², which is smaller compared to other compact wideband antennas available in existing literatures. The compactness of the proposed structure with standard gain levels makes the antenna a suitable candidate for wideband communication purpose.

ACKNOWLEDGMENT

The authors would like to express sincere gratitude to Dr. Pranab Paul of Microline India, Kolkata for extending his help in fabrication and measurement facilities.

REFERENCES

- [1] J. Gemio, J. P. Granados, and J. S. Castany, "Dual band antenna with fractal based ground plane For WLAN applications," *IEEE Antennas and Wireless Propagation Letters*, vol. 8, pp. 748-751, 2009.
- [2] R. Ghatak, R. K. Mishra, and D. R. Poddar, "Perturbed Sierpinski carpet antenna with CPW feed for IEEE 802.11 A/B WLAN application," *IEEE Antennas and Wireless Propagation Letters*, vol. 7, pp. 742-744, 2008.
- [3] W. Chen, G. Wang, and C. Zhang, "Bandwidth enhancement of a microstrip-line-fed printed wide-slot antenna with a fractal-shaped slot," *IEEE Transactions on Antennas and Propagation*, vol. 57, no. 7, pp. 2176-2179, 2009.
- [4] K. C. Hwang, "Broad band circularly-polarised Spidron fractal slot antenna," *Electronics Letters*, vol. 45, no. 1, pp. 3-4, January 1, 2009.
- [5] Y. K. Choukiker and S. K. Behera, "Design of wideband fractal antenna with combination of fractal geometries," *International Conference on Information, Communications and Signal Processing*, pp. 1-3, 2011.
- [6] B. Roy, A. Bhattacharya, S. K. Chowdhury, and A. K. Bhattacharjee, "Wideband snowflake slot antenna using Koch iteration technique for wireless and C-band applications," *AEU - International Journal of Electronics and Communications, Elsevier*, vol. 70, iss. 10, pp. 1467-1472, 2016.
- [7] S. Rosaline and S. Raghavan, "Metamaterial-inspired split ring monopole antenna for WLAN applications," *ACES Express Journal*, vol. 1, no. 5, pp. 153-156, May 2016.

INFORMATION FOR AUTHORS

PUBLICATION CRITERIA

Each paper is required to manifest some relation to applied computational electromagnetics. **Papers may address general issues in applied computational electromagnetics, or they may focus on specific applications, techniques, codes, or computational issues.** While the following list is not exhaustive, each paper will generally relate to at least one of these areas:

1. **Code validation.** This is done using internal checks or experimental, analytical or other computational data. Measured data of potential utility to code validation efforts will also be considered for publication.
2. **Code performance analysis.** This usually involves identification of numerical accuracy or other limitations, solution convergence, numerical and physical modeling error, and parameter tradeoffs. However, it is also permissible to address issues such as ease-of-use, set-up time, run time, special outputs, or other special features.
3. **Computational studies of basic physics.** This involves using a code, algorithm, or computational technique to simulate reality in such a way that better, or new physical insight or understanding, is achieved.
4. **New computational techniques** or new applications for existing computational techniques or codes.
5. **“Tricks of the trade”** in selecting and applying codes and techniques.
6. **New codes, algorithms, code enhancement, and code fixes.** This category is self-explanatory, but includes significant changes to existing codes, such as applicability extensions, algorithm optimization, problem correction, limitation removal, or other performance improvement. **Note: Code (or algorithm) capability descriptions are not acceptable, unless they contain sufficient technical material to justify consideration.**
7. **Code input/output issues.** This normally involves innovations in input (such as input geometry standardization, automatic mesh generation, or computer-aided design) or in output (whether it be tabular, graphical, statistical, Fourier-transformed, or otherwise signal-processed). Material dealing with input/output database management, output interpretation, or other input/output issues will also be considered for publication.
8. **Computer hardware issues.** This is the category for analysis of hardware capabilities and limitations of various types of electromagnetics computational requirements. Vector and parallel computational techniques and implementation are of particular interest.

Applications of interest include, but are not limited to, antennas (and their electromagnetic environments), networks, static fields, radar cross section, inverse scattering, shielding, radiation hazards, biological effects, biomedical applications, electromagnetic pulse (EMP), electromagnetic interference (EMI), electromagnetic compatibility (EMC), power transmission, charge transport, dielectric, magnetic and nonlinear materials, microwave components, MEMS, RFID, and MMIC technologies, remote sensing and geometrical and physical optics, radar and communications systems, sensors, fiber optics, plasmas, particle accelerators, generators and motors, electromagnetic wave propagation, non-destructive evaluation, eddy currents, and inverse scattering.

Techniques of interest include but not limited to frequency-domain and time-domain techniques, integral equation and differential equation techniques, diffraction theories, physical and geometrical optics, method of moments, finite differences and finite element techniques, transmission line method, modal expansions, perturbation methods, and hybrid methods.

Where possible and appropriate, authors are required to provide statements of quantitative accuracy for measured and/or computed data. This issue is discussed in “Accuracy & Publication: Requiring, quantitative accuracy statements to accompany data,” by E. K. Miller, ACES Newsletter, Vol. 9, No. 3, pp. 23-29, 1994, ISBN 1056-9170.

SUBMITTAL PROCEDURE

All submissions should be uploaded to ACES server through ACES web site (<http://aces-society.org>) by using the upload button, Express Journal section. Only pdf files are accepted for submission. The file size should not be larger than 6MB, otherwise permission from the Editor-in-Chief should be obtained first. Automated acknowledgment of the electronic submission, after the upload process is successfully completed, will be sent to the corresponding author only. It is the responsibility of the corresponding author to keep the remaining authors, if applicable, informed. Email submission is not accepted and will not be processed.

EDITORIAL REVIEW

In order to ensure an appropriate level of quality control, papers are peer reviewed. They are reviewed both for technical correctness and for adherence to the listed guidelines regarding information content and format.

PAPER FORMAT

Only camera-ready electronic files are accepted for publication. The term **“camera-ready”** means that the material is neat, legible, reproducible, and in accordance with the final version format listed below.

The following requirements are in effect for the final version of an ACES Express Journal paper:

1. The paper title should not be placed on a separate page. The title, author(s), abstract, and (space permitting) beginning of the paper itself should all be on the first page. The title, author(s), and author affiliations should be centered (center-justified) on the first page. The title should be of font size 14 and bolded, the author names should be of font size 12 and bolded, and the author affiliation should be of font size 10 (regular font, neither italic nor bolded).
2. An abstract is required. The abstract should be a brief summary of the work described in the paper. It should state the computer codes, computational techniques, and applications discussed in the paper (as applicable) and should otherwise be usable by technical abstracting and indexing services. The word "Abstract" has to be placed at the left margin of the paper, and should be bolded and italic. It also should be followed by a hyphen (–) with the main text of the abstract starting on the same line.
3. All section titles have to be centered and all the title letters should be written in caps. The section titles need to be numbered using roman numbering (I. II.)
4. Either British English or American English spellings may be used, provided that each word is spelled consistently throughout the paper.
5. Internal consistency of references format should be maintained. As a guideline for authors, we recommend that references be given using numerical numbering in the body of the paper (with numerical listing of all references at the end of the paper). The first letter of the authors' first name should be listed followed by a period, which in turn, followed by the authors' complete last name. Use a comma (,) to separate between the authors' names. Titles of papers or articles should be in quotation marks (" "), followed by the title of the journal, which should be in italic font. The journal volume (vol.), issue number (no.), page numbering (pp.), month and year of publication should come after the journal title in the sequence listed here.
6. Internal consistency shall also be maintained for other elements of style, such as equation numbering. Equation numbers should be placed in parentheses at the right column margin. All symbols in any equation have to be defined before the equation appears or right immediately following the equation.
7. The use of SI units is strongly encouraged. English units may be used as secondary units (in parentheses).
8. Figures and tables should be formatted appropriately (centered within the column, side-by-side, etc.) on the page such that the presented data appears close to and after it is being referenced in the text. When including figures and tables, all care should be taken so that they will appear appropriately when printed in black and white. For better visibility of paper on computer screen, it is good to make color figures with different line styles for figures with

multiple curves. Color should also be tested to insure their ability to be distinguished after black and white printing. Avoid the use of large symbols with curves in a figure. It is always better to use different line styles such as solid, dotted, dashed, etc.

9. A figure caption should be located directly beneath the corresponding figure, and should be fully justified.
10. The intent and meaning of all text should be clear. For authors who are not masters of the English language, the ACES Editorial Staff will provide assistance with grammar (subject to clarity of intent and meaning). However, this may delay the scheduled publication date.
11. Unused space should be minimized. Sections and subsections should not normally begin on a new page.

ACES reserves the right to edit any uploaded material, however, this is not generally done. It is the author(s) responsibility to provide acceptable camera-ready files in pdf and MSWord formats. Incompatible or incomplete files will not be processed for publication, and authors will be requested to re-upload a revised acceptable version.

COPYRIGHTS AND RELEASES

Each primary author must execute the online copyright form and obtain a release from his/her organization vesting the copyright with ACES. Both the author(s) and affiliated organization(s) are allowed to use the copyrighted material freely for their own private purposes.

Permission is granted to quote short passages and reproduce figures and tables from an ACES Express Journal issue provided the source is cited. Copies of ACES Express Journal articles may be made in accordance with usage permitted by Sections 107 or 108 of the U.S. Copyright Law. The consent does not extend to other kinds of copying, such as for general distribution, for advertising or promotional purposes, for creating new collective works, or for resale. The reproduction of multiple copies and the use of articles or extracts for commercial purposes require the consent of the author and specific permission from ACES. Institutional members are allowed to copy any ACES Express Journal issue for their internal distribution only.

PUBLICATION CHARGES

There is a \$200 basic publication charge assigned to each paper for ACES members, and \$300 charge for non-ACES members. Corresponding authors should be active members of the society at the time of submission and the time of publication in order to receive the reduced charge.

ACES Express Journal doesn't allow for more than four pages. All authors must comply with the page limitations. ACES Express Journal is an online journal, and printed copies are not available.

Upon completion of its first year, ACES Express Journal will be abstracted in INSPEC, in Engineering Index, DTIC, Science Citation Index Expanded, the Research Alert, and to Current Contents/Engineering, Computing & Technology.